




Cite this: *Polym. Chem.*, 2017, **8**, 2979

Molecular design through computational simulation on the benzo[2,1-*b*;3,4-*b'*]dithiophene-based highly ordered donor material for efficient polymer solar cells†

Sung Jae Jeon, Seung Jun Nam, Yong Woon Han, Tae Ho Lee and Doo Kyung Moon *

Donor–acceptor (D–A) copolymers have been proved to be excellent candidates for efficient polymer solar cells (PSCs). An easy and powerful strategy of D–A copolymer design to enhance the performance of PSCs would advance their industrialization. Here we demonstrate an effective molecular design method using the simple molecular mechanics function of MM2 (Molecular Mechanic program 2) & MMFF94 (Merck Molecular Force Field 94) calculation and noncovalent conformational locking effects in the D–A polymer backbone. It is shown to play an important role in D–A copolymers with a highly ordered structure through intra- and/or intermolecular interactions. We report a newly designed D–A copolymer donor, poly(benzodithiophene-dibenzophenazine), P(BDP-DTPz), using our strategy which exhibits good solubility, high molecular ordering and excellent charge carrier mobility balance. A maximum power conversion efficiency (PCE) of 6.2% is achieved with a P(BDP-DTPz):PC₇₁BM blend under 1.5 G solar irradiation. This work will provide a new perspective for molecular design of D–A copolymers in PSCs.

Received 19th February 2017,
Accepted 30th March 2017

DOI: 10.1039/c7py00292k

rsc.li/polymers

1. Introduction

Polymer solar cells (PSCs) are in the spotlight as a potential technology for the development of flexible and portable photo-voltaic devices because of their superior mechanical flexibility and ability to allow low-cost solution processing on a plastic substrate.^{1–3} Lately, bulk heterojunction (BHJ) polymer solar cells consisting of polymer donor–fullerene acceptor blends have been reported to exhibit high power conversion efficiencies (PCEs) of greater than 9–11%.^{4–6} Most polymer donor–fullerene acceptor BHJ blends display a limited exciton diffusion length of 10–20 nm. Thus, in order to obtain highly efficient PSCs, a fine morphology that forms an interpenetrating donor–acceptor network is necessary.^{7–10} The morphology of BHJ blends can be partially adjusted through film formation processes, which control the miscibility of the polymer and fullerene materials. However, because this is determined by

the intrinsic properties of the donor polymer, the molecular design of the donor polymer becomes highly important.^{11–14}

Most donor polymers are designed by using alternating electron donor (D)–electron acceptor (A) orbital mixing.^{4,5,15,16} This method is effective for producing π -conjugated copolymers with low electronic band gaps and it enables production of polymers with high photon harvesting efficiencies.¹⁷ However, the intermolecular interactions of the polymer as well as the intramolecular interactions between the polymer and fullerene also need to be considered to achieve high-efficiency PSCs.

Steric hindrance must be minimized by controlling the side chains^{18–21} of the donor and acceptor units in the polymer backbone, including their substituents,¹¹ length,⁵ position,²² and contents.²³ Also, considering the miscibility²⁴ of the polymer backbone with fullerene, a planar curvature that allows smooth charge transfer should be attained, in order to secure the desired interpenetrating regions.^{6,25}

Many groups including that of Youyoung Li have used geometry optimization software such as Gaussian, Jaguar quantum chemistry, and Material Studio to consider and compute the curvature and planarity of the molecular structure.^{26–28} In 2010, Klaus Mullen performed structure analysis with a simple force-field optimization using MMFF on copolymers of benzodithiophene isomers and alkyl-substituted

Nano and Information Materials (NIMs) Laboratory, Department of Materials Chemistry and Engineering, Konkuk University, 120, Neungdong-ro, Gwangjin-gu, Seoul 05029, Korea. E-mail: dkmooon@konkuk.ac.kr; Fax: +82-2-444-0765; Tel: +82-2-450-3498

†Electronic supplementary information (ESI) available. See DOI: 10.1039/c7py00292k

bithiophene. The synthesized polymers were reported to possess various properties including solubility, electronic levels, morphology in a film, and charge carrier mobility on organic field-effect transistors, all of which varied depending on polymer backbone curvatures.²⁹

In 2014, H. Y. Woo reported copolymers of difluorobenzothiadiazole and dialkoxy-phenylene derivatives that exhibited high efficiencies of greater than 9%. This has been explained by the improved planarity of the optimized conformation when strongly electronegative fluoro and oxygen substituents were introduced into the molecular structure, enabling noncovalent conformational locking with hydrogen, nitrogen, and sulfur atoms.³⁰

In this study, the D–A interaction of a donor polymer was controlled and a planar curvature was achieved by using the simple molecular mechanics function of MM2 & MMFF94 as well as noncovalent conformational locking effects.^{31,32} Also, the following molecular design strategies were developed to create a D–A copolymer with an optimal planar geometry.

- Planar donor unit with high charge carrier mobility:

Benzo[2,1-*b*:3,4-*b'*]dithiophene (BDP)^{33,34}

- Strong acceptor unit with high planarity:

Dibenzo[*a,c*]phenazine (Pz)^{35,36}

- Introduction of spacers, side chains, and substituents to minimize D–A steric hindrance

It was verified that the molecular behavior of a D–A copolymer, designed as described above based on BDP and Pz units, P(BDP-DTPz) closely matched the curvatures (repeating unit, $n = 1, 2, 4$) predicted and calculated by MM2 & MMFF94 and the Gaussian 09-computed results. The P(BDP-DTPz) structure demonstrated by ¹H NMR data, X-ray diffraction (XRD) and grazing incidence wide angle X-ray scattering (GI-WAXS) measurements on the synthesized P(BDP-DTPz) confirmed the dominance of the face-on orientation on the substrate, indicating the planar rigid structure of the polymer backbone.³⁷ We found that an optimized device of P(BDP-DTPz):PC₇₁BM = 1:1.5 with balanced charge carrier mobility showed a maximum PCE of 6.2% for PSCs. This polymer study is expected to offer interesting information regarding the molecular design of D–A combinations.

2. Results and discussion

2.1 Instruments and characterization

Unless otherwise specified, all reactions were performed under a nitrogen atmosphere. The solvents were dried using the standard procedures. All column chromatography experiments were performed with silica gel (230–400 mesh, Merck) as the stationary phase. ¹H NMR spectra were collected by using a Bruker ARX 400 spectrometer using solutions in CDCl₃ with chemical concentrations recorded in ppm units using TMS as the internal standard. Elemental analysis (EA) was performed with a Thermofinnigan EA2000. The electronic absorption spectra were measured in chloroform using an HP Agilent 8453 UV-Vis spectrophotometer. The cyclic voltammetry waves

were obtained using a Zahner IM6eX electrochemical workstation with a 0.1 M acetonitrile (purged with nitrogen for 20 min) solution containing tetrabutylammonium hexafluorophosphate (Bu₄NPF₆) as the electrolyte at a constant scan rate of 50 mV s⁻¹. ITO, a Pt wire, and silver/silver chloride [Ag in 0.1 M KCl] were used as the working, counter, and reference electrodes, respectively. The electrochemical potential was calibrated against Fc/Fc⁺. The highest occupied molecular orbital (HOMO) levels of the polymers were determined using the oxidation onset value. The onset potentials are the values obtained from the intersection of the two tangents drawn at the rising current and the baseline changing current of the CV curves. Thermogravimetric analysis (TGA) measurements were performed on a NETZSCH TG 209 F3 thermogravimetric analyzer. All gel permeation chromatography (GPC) analyses were performed using THF as an eluent and a polystyrene standard as a reference. XRD patterns were obtained using a Smart Lab 3 kW (40 kV, 30 mA, Cu target, wavelength: 1.541871 Å) instrument from Rigaku, Japan. GI-WAXS measurements were conducted at the PLS-II 6D UNIST-PAL beamline of the Pohang Accelerator Laboratory (PAL) in Korea. The X-rays coming from the bending magnet are monochromated using Si(111) double crystals and focused at the detector position using a toroidal mirror. Grazing incidence wide angle X-ray scattering (GI-WAXS) patterns were recorded with a 2D CCD detector (MX225-HS, Rayonix L.L.C., USA) and the X-ray irradiation time was 60 seconds depending on the saturation level of the detector. Diffraction angles were calibrated by using a pre-calibrated sucrose (monoclinic, P21, $a = 10.8631$ Å, $b = 8.7044$ Å, $c = 7.7624$ Å, $\beta = 102.938^\circ$) and the sample-to-detector distance was about 240 mm. Topographic images of the active layers were obtained through atomic force microscopy (AFM) in a tapping mode under ambient conditions using an XE-100 instrument. The molecular geometries of the model molecules were obtained by minimize energy calculations (MM2 & MM94) with ChemBio3D Ultra 11.0 (CambridgeSoft). Theoretical analyses were performed using density functional theory (DFT), as approximated by the B3LYP functional and employing the 6-31G/ basis set in Gaussian 09.

2.2 Fabrication and characterization of PSCs

All the BHJ photovoltaic cells were prepared using the following device fabrication procedure. Indium tin oxide (ITO) glass (10× sq⁻¹, Samsung corning) was sequentially sonicated using a detergent (Alconox in deionized water, 10%), acetone, isopropyl alcohol, and deionized water for a period of 20 min. The moisture was thoroughly removed under an N₂ gas flow. To ensure the complete removal of the remaining water, the ITO glass was heated on a hot plate for 10 min at 100 °C. For the hydrophilic treatment of the ITO glass surface, the glass was cleaned for 10 min in a UVO cleaner, and poly(3,4-ethylenedioxythiophene):poly(styrene-sulfonate) (PEDOT:PSS, Clevious P VP AI 4083) was passed through a 0.45 μm filter before being deposited onto the ITO glass to produce a 50 nm thick layer by spin-coating at 4000 rpm. The coated glass was then dried at 120 °C for 20 min inside a glove box. Composite solutions of

the polymer and PC₇₁BM were prepared using *o*-dichlorobenzene (*o*-DCB). The solutions were filtered through a 0.45 μm polytetrafluoroethylene (PTFE) filter and then spin-coated (1000–4000 rpm, 30 s) on top of the PEDOT:PSS layer. The conventional/inverted device fabrication was completed by depositing thin layers of Ba (2 nm), and Al (100 nm)/ZnO (or ZnO + PFN) (~10 nm) instead of a PEDOT:PSS layer, MoO₃ (2 nm) and Al (100 nm) at pressures of less than 1026 Torr. The active area of the device was 0.04–0.12 cm². Finally, the cell was encapsulated using UV-curing glue (Nagase, Japan). The output photocurrent was adjusted to match the photocurrent of the Si reference cell to obtain a power density of 100 mW cm⁻². After encapsulation, all devices were operated under an ambient atmosphere.

2.3 Polymerization

Scheme 1 outlines the synthetic route to the polymer. The detailed synthetic procedures and characterization results for the monomers (M1 and M2) are presented in the ESI (see Fig. S1–S4†).

2.4 P(BDP-DTPz)

Pz monomer (M2) (172 mg, 0.2 mmol), tris(dibenzylideneacetone)dipalladium(0) (7.32 mg, 0.008 mmol) and tri(*o*-tolyl)phosphine (9.73 mg, 0.032 mmol) were dissolved in toluene (12 mL). The flask was degassed and refilled with nitrogen gas twice, and then BDP monomer (M1) (154.5 mg, 0.2 mmol) was added to the mixture. The flask was degassed and refilled twice. The polymerization mixture was stirred at 90 °C for 60 h, and a few drops of 2-bromothiophene were added. After 3 hours, a few drops of 2-tributylstannyl thiophene were also added for the end-capping reaction. The reaction mixture was cooled to room temperature and poured into methanol. The precipitate was filtered and purified with methanol, acetone, hexane, and chloroform in Soxhlet apparatus. The polymer was filtered through Celite and re-precipitated in methanol. Finally, the polymer was collected as a dark brown solid (70%, 160.4 mg). ¹H NMR (400 MHz, CDCl₃, δ): 8.62–8.59 (br, 2H), 8.31–8.23 (br, 2H), 7.84–7.82 (br, 4H), 7.75–7.69 (br, 4H), 7.56–7.52 (br, 2H), 4.17–4.08 (br, 4H), 1.95–1.93 (br, 2H), 1.37–1.31 (br, 10H), 1.07–0.88 (br, 24H). Anal. calcd for C₇₀H₈₄N₂O₄S₄: C, 73.38; H, 7.39; N, 2.45; O, 5.59; S, 11.20; EA, Found (%): C, 72.64; H, 7.22; N, 1.78; O, 5.16; S, 11.26.

3. Results and discussion

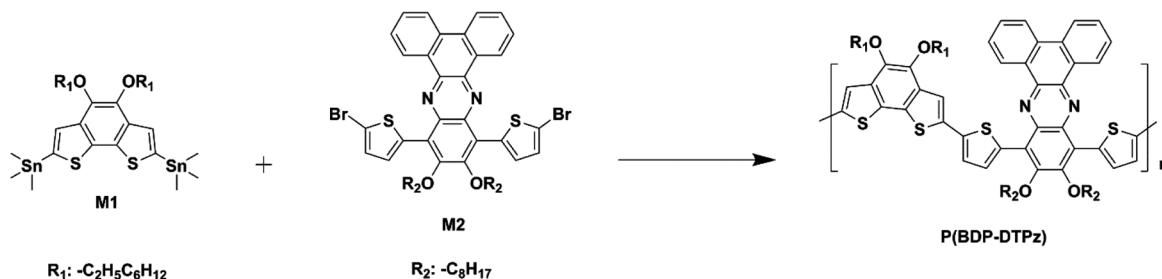
3.1 Polymer design and characterization

3.1.1 Design of P(BDP-DTPz). As shown in Scheme 1, benzo[2,1-*b*:3,4-*b'*]dithiophene (BDP), a structural isomer of BDT with improved charge carrier mobility, was selected for the donor (M1). In addition, alkoxy side chains were introduced into the central benzene to provide high miscibility with fullerene derivatives. This led to a planar curvature very similar to BDT, which is highly advantageous when forming large planar conjugated structures, leading to high charge carrier mobility³⁸ and π - π stacking during polymerization, improving thin film transistor (TFT) properties by a factor of 100.²⁹ However, due to the asymmetric nature of BDP, proper selection of the acceptor group after considering the regioregularity can improve the degree of polymerization.

Dibenzo[*a,c*]phenazine (Pz), a phenazine derivative, was selected for the acceptor (M2). Phenazine has lower electron withdrawing strength than benzothiadiazole and quinoxaline, but has a further extended π -system with a stabilized structure that can lower the HOMO level of polymer.³⁹ Introducing the phenanthrene core maximized the planarity of phenazine, and alkoxy side chains were used to achieve high solubility.

Finally, thiophene (Th) spacers were introduced to minimize steric hindrance inside the D–A copolymer backbone and to increase charge carrier mobility. Introducing the Th spacers not only improved the mobility but also reduced the large tilting angle between the D–A units,³⁹ and a locking structure from the noncovalent interactions of the oxygen substituents on the Pz unit was also expected.⁴⁰ The space provided by the Th spacers between the donor and acceptor units also led to a high degree of polymerization.³⁹ Furthermore, the alkoxy side chains on the two units were expected to lead to acceptable solubility as well as formation of highly ordered films inside and outside of the backbone due to noncovalent conformational locking.

3.1.2 Characterization of P(BDP-DTPz). The P(BDP-DTPz) of the designed D–A copolymer was synthesized by the Stille coupling polymerization of the stannylated monomer M1 and brominated M2 in 70% yield in the presence of Pd₂(dba)₃/P(*o*-tol)₃ as a catalyst in anhydrous toluene. The resulting polymer was purified by Soxhlet extraction with methanol, acetone, hexane and chloroform, and the portion dissolved in chloroform was filtered through Celite and re-precipitated into



Scheme 1 Synthetic route of P(BDP-DTPz).

methanol. The polymer is readily soluble in common organic solvents such as dichloromethane, chloroform, chlorobenzene, and *o*-DCB. The molecular weight of the polymer was determined by GPC using THF as eluent at room temperature. The weight-average molecular weight (M_w) is 32 542 g mol⁻¹ (PDI = 3.10). The polymer exhibited high thermal stability at a decomposition temperature of 334 °C (with 5% weight loss) through TGA (see Fig. S5†).

3.2 Prediction of polymer structure through computational calculations (MM2 & MMFF94)

As shown in Scheme 2, P(BDP-DTPz) has elements including oxygen, sulfur, nitrogen, and hydrogen in its molecular structure. It was designed to operate with a noncovalent bonding interaction between neighboring elements. On a 2-dimensional plane, a polymer of a repeating unit (n), $n = 2$, largely has 5 possible curvatures (a)–(e) depending on the side chain direction of the BDP donor and the Pz acceptor. However, due to the structural locking effect, structure (a) is expected to be dominant in the actual polymer.²⁸

To see if the curvature in Scheme 2(a) was related to the molecular design strategies, a molecular force-field optimization was performed using a simple, fast MM2 & MMFF94 computation. As shown in Fig. 1, MM2 & MMFF94 was used to obtain the optimized geometry of each repeating segment of P(BDP-DTPz), and the most stable structure was found by performing an energy scan according to the change in the torsion angle between neighboring units. All side chains within the structure were simplified as methoxy groups to minimize the computational time and error (see ESI†).

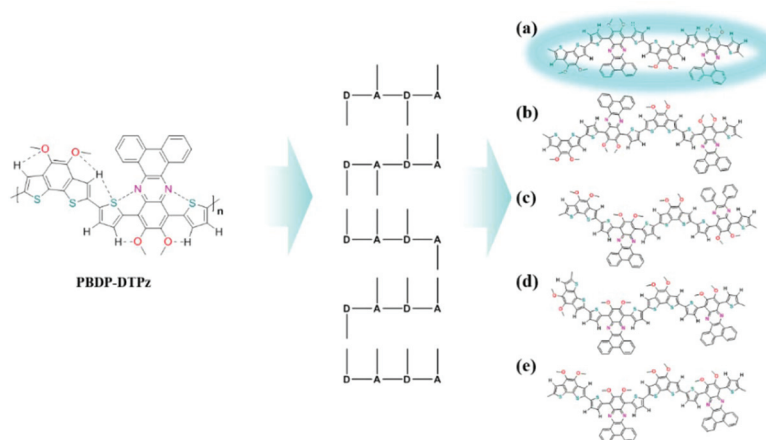
BDP was most energetically stable in the conformation shown in Fig. 1(a), with a conformational energy of 36.616 kcal mol⁻¹ (by MM2). When thiophene was combined with BDP (BDP-Th), structure (b) appears to be the most stable at 49.917 kcal mol⁻¹ (by MM2). To investigate which torsion angle between BDP and Th (right) was the most stable, a dihedral driver showing the relationship between the torsion angle and conformational energy was used. As shown in (c), a

conformational energy of 49.69 kcal mol⁻¹ demonstrated that the most stable structure was at a torsion angle of -155° after tilting by 25°. The same calculation was performed when thiophene was introduced at the 2 and 7 positions of BDP (Th-BDP-Th, left). As shown in (d) and (e), a stable structure occurred with a conformational energy of 62.668 kcal mol⁻¹ (by MM2), and the most stable structure appeared at a tilting angle of -155° in the dihedral driver, with a conformational energy of 62.49 kcal mol⁻¹.

The interaction between Pz and a neighboring thiophene was calculated in the same way as that used for BDP. As shown in Fig. 1(f), a stable structure with an energy of 3.3819 kcal mol⁻¹ (by MM2) was obtained. When thiophene was combined with Pz (Pz-Th, right), structure (g) was the most stable, with a conformational energy of 20.619 kcal mol⁻¹ (by MM2). Next, the dihedral driver (h) between Pz and Th (right) confirmed that the most stable structure had a conformational energy of 20.15 kcal mol⁻¹ at a torsion angle of -125°. When thiophene was introduced at both the 10 and 13 positions of phenazine (Th-Pz-Th, left), a stable structure with an energy of 42.1597 kcal mol⁻¹ (by MM2) was predicted, as shown in (i) and (j), and the most stable conformation (42.02 kcal mol⁻¹) was revealed to occur at a torsion angle of -85° by the dihedral driver.

The polymer structure was calculated by using computed structures when $n = 1$ and 2. However, MM2 could not find a stable structure for the polymer with the lowest energy. This was caused by a difference between the conformational energy calculations using MM2 and the dihedral driver, meaning that the value obtained using MM2 was higher than that provided by the dihedral driver. However, the most stable structure was found by additional computation of MMFF94 on top of MM2 and application of the dihedral driver method.

As shown in Fig. 1(k), P(BDP-DTPz) ($n = 1$) returned a stable structure at 274.938 kcal mol⁻¹ (by MMFF94) after computation of MM2 and the dihedral driver method (see ESI†). The most stable conformation obtained by the dihedral driver calculations between BDP and thiophene (right) of Pz, which had



Scheme 2 Concept of the P(BDP-DTPz) design of polymers and their curvatures of $n = 2$; (a)–(e).

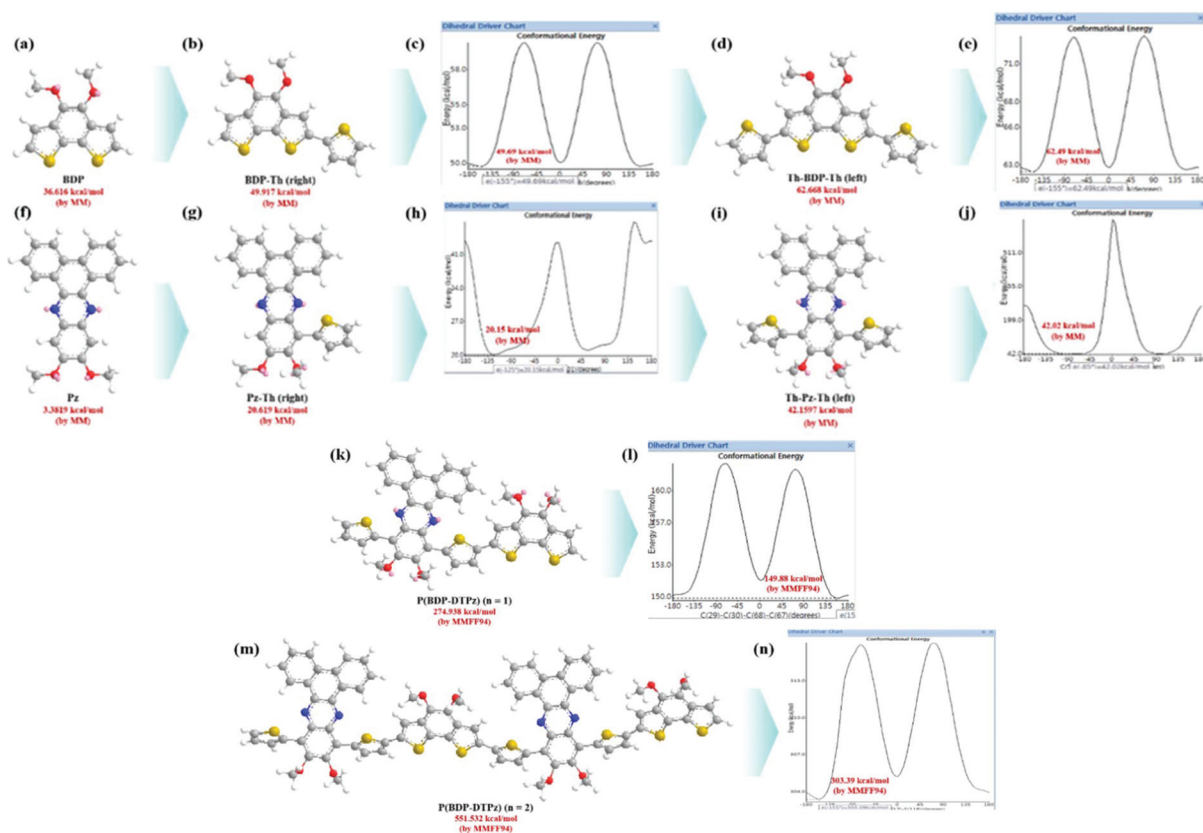


Fig. 1 The total energy scan of the rotamers of the adjacent molecular units and the chemical structures of $n = 1, 2$ in the polymer using MM2 & MMFF94.

an energy of $149.88 \text{ kcal mol}^{-1}$, was obtained at a torsion angle of -155° , as in (l). P(BDP-DTPz) ($n = 2$) underwent computation using the same method, showing a stable structure with an energy of $551.532 \text{ kcal mol}^{-1}$ (by MMFF94), as shown in (m). Lastly, the most stable structure between the BDP unit and the Pz-Th unit (left) of P(BDP-DTPz) ($n = 1$) obtained using the dihedral driver method was found at a torsion angle of -155° , with a conformational energy of $303.39 \text{ kcal mol}^{-1}$, as shown in (n). The curvature of P(BDP-DTPz) ($n = 2$) was calculated by using MM2 & MMFF94 as shown Scheme 2.

3.3 Prediction of the polymer structure through computational calculation (Gaussian 09)

This section explores whether the curvature of the polymer calculated using the MM2 & MMFF94 function matches that calculated using Gaussian 09. The alkoxy chains on the alkoxy-phenazine and alkoxy-BDP core building blocks of the polymer were simplified to methoxy to reduce computational time. Next, the optimized geometry was calculated using density functional theory (DFT) computation with the B3LYP/6-31g(d) basis set. After this, a total of 18 steps of minimized energy states were calculated from 0° to 180° with 10° increments using the B3LYP/6-31g(d) basis set.²⁷

Fig. 2(a) describes the total energy of each segment in BDP-Th, Pz-Th(R), and Th(L)-Pz-Th at different torsion angles, while (b) shows the normalized total energy data for each

torsion angle. These results demonstrate that the three rotatable segments show very different barriers for rotation, *i.e.*, $3.258 \text{ kcal mol}^{-1}$, $1.957 \text{ kcal mol}^{-1}$, and $2.477 \text{ kcal mol}^{-1}$ for BDP-Th, Pz-Th(R), and Th(L)-Pz-Th, respectively. The rotation angle between the maximum energy barrier (with energetically unstable conformation) and the minimum energy barrier (with optimum conformation).^{41–43}

As shown in Fig. 2(a), the most stable structure of BDP-Th (black line) ($3.177 \text{ kcal mol}^{-1}$) occurs at a torsion angle of 20° between thiophene and the neighboring BDP. Pz-Th(R) (red line) has low energy when the torsion angle between phenazine and Th(R) is either 0° or 180° , with the energy at 0° ($0.168502 \text{ kcal mol}^{-1}$) being calculated to be slightly more stable than that at 180° ($0.164329 \text{ kcal mol}^{-1}$). Th(L)-Pz-Th (blue line), in which Th is connected to both sides of Pz, revealed a stable structure ($2.90515 \text{ kcal mol}^{-1}$) at a torsion angle of 30° between phenazine and Th(L). The geometry optimization results for $n = 1$ and 2 after entering the output values as displayed in Fig. 2(c) showed a polymer curvature that was highly similar to those shown in Fig. 1(k) and (m), *i.e.*, the results from the MM2 & MMFF94 function.

The structure of Pz-Th(R) was a result of both the noncovalent S...N interaction between S in Th and N in Pz and the hydrogen bonding ($\text{H}\cdots\text{O}$) between the proton at the 3 position of Th and the O on the alkoxy side chain at the 6 position of Pz, as well as the hydrogen bonding ($\text{H}\cdots\text{N}$) between H in Th

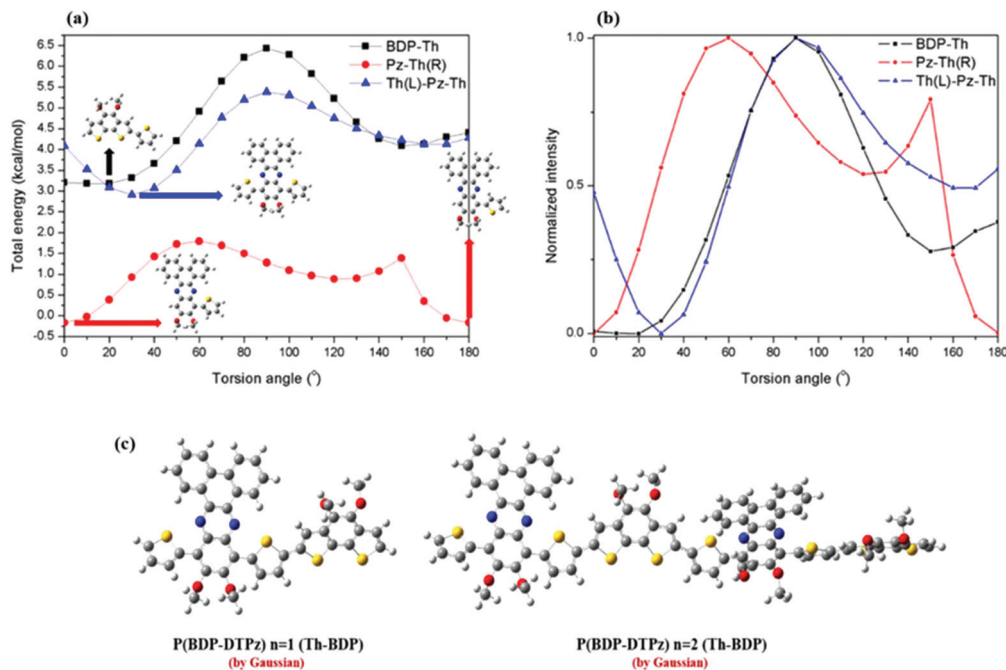


Fig. 2 The total energy scan of the rotamers of the adjacent molecular units and the chemical structures of $n = 1, 2$ in the polymer using Gaussian 09.

and N in Pz and the noncovalent S...O interaction between S in Th and O in Pz.^{10,30,37,40,44,45} As seen from the red line of (a), if Th was only added to one side of the Pz core (right), the structure with a torsion angle of 0° (S direction: up) was more stable than that with an angle of 180° (S direction: down), with their energies being -0.168502 kcal mol⁻¹ and 0.004173 kcal mol⁻¹, respectively.

The results were different when comparing one side of Th (L)-Pz-Th to the other. Two sets of forces were analyzed by comparing the electronegativity difference or the hydrogen bonding strength. Because the electronegativity follows the order F (4.0) > O (3.5) > N (3.0) > S (2.5) > ... > H (2.1), and since hydrogen bonding is the strongest noncovalent interaction, the strongest attractive force was for H...O.⁴⁶ The

energy scan result for Th(L)-Pz-Th, represented as the blue line in (a), showed a stabilized structure with Th in the up direction at an angle of 30° and an energy of 2.90515 kcal mol⁻¹. This can be explained by the H...O hydrogen bonding interaction in the up-direction being stronger than the H...N interaction in the down-direction. When the distances between the elements were obtained by Gaussian 09, the H...O distance (2.359 Å) was found to be smaller than the H...N distance (2.473 Å), showing that the noncovalent interaction of H...O was stronger than that of H...N.

3.4 The DFT calculations

As shown in Fig. 3, the chemical structure of the polymer and the optimal geometry with the HOMO and lowest occupied

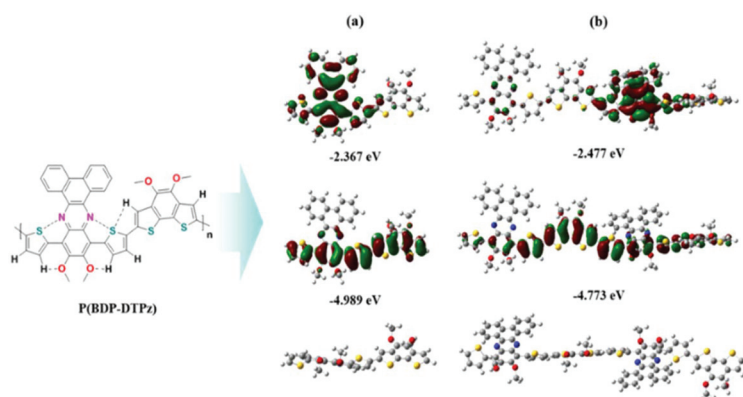


Fig. 3 DFT calculation data of the polymer: (a) P(BDP-DTPz), $n = 1$, and LUMO/HOMO/side view, and (b) P(BDP-DTPz), $n = 2$, and LUMO/HOMO/side view.

molecular orbital (LUMO) surfaces of their conjugated backbones obtained from theoretical calculation by DFT at the B3LYP/6-31G(d) basis set. The computational results displayed in Fig. 3(a) and (b) show that the HOMO was predicted to be evenly delocalized along the polymer backbone, while the LUMO showed electron clouds concentrated on the Pz acceptor units, in the case of the LUMO, predicting high electron mobility across the polymer backbone.

The regular arrangement of the D-A units in the polymer backbone was verified, with alkoxy side chains alternating in the downward (D) and upward (A) positions. In addition, the tilting angles of BDP-Th and Pz-Th were 20° and 30°, respectively, and the polymer revealed twist growth as shown in the side views of Fig. 3(a) and (b). A sign of a strong side-chain group stacking interaction in neighboring units was expected from such a result, similar to the TQ1 polymer.⁴⁷

3.5 Comparing polymer curvatures as calculated using MM2 & MMFF94 and Gaussian 09

Fig. 4 shows the curvature calculated using MM2 & MMFF94 and using Gaussian 09 when the polymer curvature was $n = 4$. A linear planar curvature as shown in (a) was found when computing with MM2 & MMFF94 optimization, whereas a linear twisted curvature as shown in (b) in the case of using Gaussian 09. Although the structures calculated using the two different tools looked slightly different, only MM2 & MMFF94 was sufficient for predicting issues such as the regularity of the body structure and the chain direction. If polymers are designed after considering the MM2 & MMFF94 function and

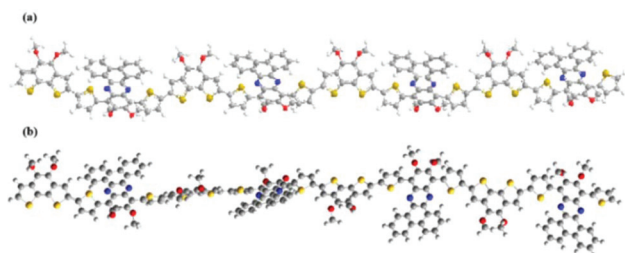


Fig. 4 Polymer curvatures ($n = 4$): (a) MM2 & MMFF94 calculation data and (b) Gaussian 09 calculation data.

noncovalent conformational locking within their molecular structure, faster and easier polymer structure prediction will be possible.

3.6 Optical and electrochemical properties

Fig. 5(a)–(c) show the UV-vis absorption spectra of the polymer solutions in chloroform and of the film on a quartz plate. P(BDP-DTPz) shows two absorption peaks; the absorption peak in the short wavelength range ($\lambda_{\max} = 415$ nm) is from the $\pi-\pi^*$ transition in the conjugated polymer backbone, and the absorption peak in the long wavelength range ($\lambda_{\max} = 531$ nm) is from a strong intramolecular charge transfer (ICT) interaction between donor and acceptor units.⁴⁸ From the graph (a) and the Beer–Lambert ($A = \epsilon bc$) equation, ϵ was calculated to be $71\,300\text{ M}^{-1}\text{ cm}^{-1}$ at 415 nm and $37\,030\text{ M}^{-1}$ at 531 nm. The $\pi-\pi^*$ transition effect in the polymer was relatively high when compared to the absorption coefficients of other BDT-based D-A copolymers.⁴⁹ On the other hand, the ICT effect was rather because of the high aromaticity of the Pz core.^{39,50} To compensate for this effect, studies have reported introduction of fluorine into the Pz core, but these studies have not shown high efficiency due to solubility issues.^{51,52} Graph (b) shows that λ_{\max} in the long wavelength range red-shifted by 45 nm from 532 nm when the polymer was in the solution state to 577 nm as a thin film in the solid state. In addition, when compared to the solution phase, the overall absorption region and intensity increased, showing signs of closed packing as the polymer became highly aggregated in the film phase. The optical band gap, obtained from the onset of the absorption spectra in the film, was estimated to be 1.80 eV. Due to the broad absorption properties of P(BDP-DTPz), moderate photo-harvesting properties were expected in devices.

The HOMO level of the polymer was measured with cyclic voltammetry (CV). The measured potential was calibrated against ferrocene, which was used as the internal standard. A polymer film was created by dropcasting the polymer dissolved in chloroform on an ITO glass electrode, which was then used as the working electrode. Measurements were performed under an N_2 atmosphere in 0.1 M Bu_4NPF_6 in acetonitrile solution. The oxidation onset potential ($E_{\text{onset}}^{\text{ox}}$) measured from the graph in Fig. 5(c) was -1.20 eV, and the electrochemical equation, $E_{\text{HOMO}} = -4.8 - (E_{\text{onset}} - E_{1/2, \text{ferrocene}})$ and the half

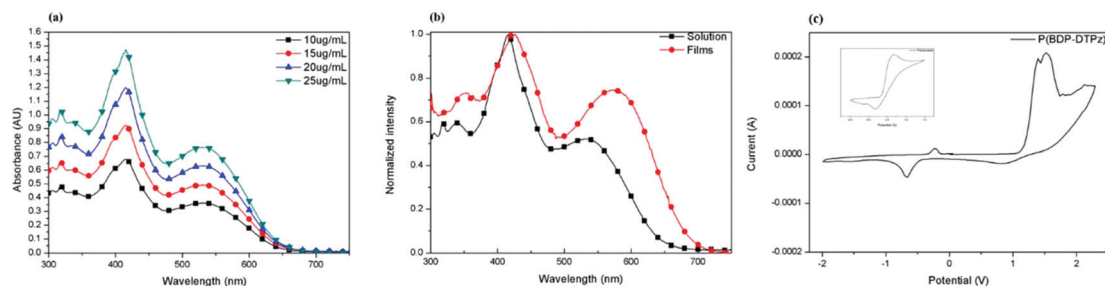


Fig. 5 Absorption spectra and the CV curve of the polymer (a) in chloroform solution ($10\text{ }\mu\text{g mL}^{-1}$ – $20\text{ }\mu\text{g mL}^{-1}$, 4 solutions of different concentrations), (b) in solution versus in film (normalized data) and (c) cyclic voltammograms of the ferrocene (in the inset) and the polymer.

wave potential of ferrocene allowed confirmation of a deep HOMO level of -5.55 eV. The HOMO level must be lower than the air oxidation threshold of -5.27 eV in order for a material to show oxidative stability.⁵³ The polymer showed superior oxidation stability with a HOMO level that was 0.33 eV lower than -5.27 eV. This can be explained by the high rigidity of BDP and the stable structure of the phenazine introduced with the phenanthrene core, and this deep HOMO level is expected to provide a superior open circuit voltage for PSCs.⁵² Furthermore, the LUMO calculated by adding the optical band gap to the HOMO level was -3.75 eV, which should allow smooth movement of electrons, with only a difference of 0.3 eV between the HOMO and the LUMO level of the fullerene acceptor.⁵⁴

3.7 Photovoltaic characteristics

PSC devices were fabricated and characterized to investigate the photovoltaic properties of P(BDP-DTPz). All devices were fabricated with the following structure – conventional cell: ITO glass/PEDOT:PSS/polymer:PC₇₁BM/Ba/Al, inverted cell: ITO glass/ZnO (or ZnO + PFN)/polymer:PC₇₁BM/MoO₃/Ag. The current density–voltage (J – V) curves and the EQE curves of the polymer are displayed in Fig. 6 and Table 1, respectively.

First, as shown in Fig. 6(a), experiments were conducted to find the optimal ratio and thickness of the 1 wt% blends of the polymer and PC₇₁BM in *o*-DCB. Conventional cells were fabricated with polymer:PC₇₁BM blend ratios from 1 : 1 to 1 : 4, with the PCEs for the 1 : 1, 1 : 1.5, 1 : 2, 1 : 3, and 1 : 4 blends being 4.5%, 4.8%, 4.0%, 3.5%, and 3.1%, respectively. An optimal thickness of 80 nm was identified by alpha-step measurement of the parts of the cells with the highest PCEs

for each ratio. Next, the polymer concentration was increased from 1 wt% to 2 wt% in order to fabricate 1 : 1 and 1 : 1.5 cells. This showed that a polymer concentration of 2 wt% led to PCEs of 4.7% for the 1 : 1 cell and 4.9% for the 1 : 1.5 cell, the highest PCE having a V_{oc} of 0.838 V, a J_{sc} of 8.7 mA cm⁻², and a FF of 65%.

In order to avoid decreased efficiency caused by poor interaction of the active layer due to acidification by PEDOT:PSS, a ZnO layer made using the sol-gel technique was introduced instead of the PEDOT:PSS layer to produce an inverted cell. The highest PCE conditions for the conventional cell (polymer:PC₇₁BM = 1 : 1.5, 2 wt% in *o*-DCB) were used to create the inverted cell, and as a result, an improved PCE of 5.1% with a V_{oc} of 0.858 V, a J_{sc} of 9.2 mA cm⁻², and a FF of 63.4% was obtained, as seen in Fig. 6(b). We introduced the previously reported ZnO–PFN hybrid interlayer to improve electron extraction in the inverted cell.⁵⁵ As shown in Fig. 6(c), the EQE was improved across the polymer's entire absorption range (300–700 nm), and the best PCE obtained was 6.2%, showing a V_{oc} of 0.859 V, a J_{sc} of 11.1 mA cm⁻², and a FF of 65.3%.

3.8 Film morphology and orientation properties

3.8.1 AFM analysis. To correlate the morphology of the active layer with device properties, the nanoscale morphology of blend films was examined by tapping mode AFM. The measured AFM data were arranged in an order of increasing PCEs, along with the topography and 3D images, as shown in Fig. 7. Fig. 7(a)–(e) show the 2D topography and 3D images of the conventional cells, while (f) shows those of the inverted cells. When devices were fabricated using P(BDP-DTPz):

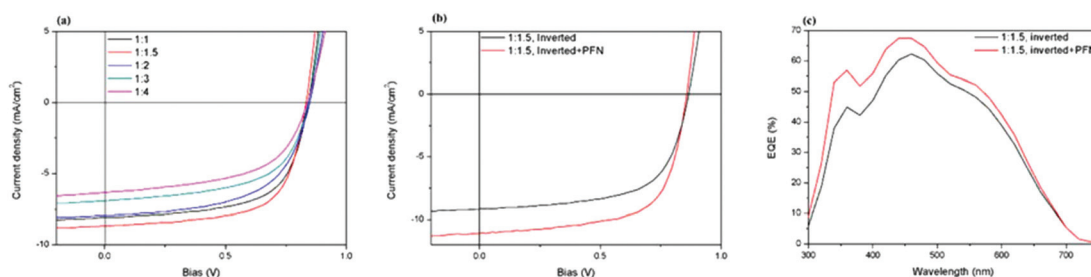


Fig. 6 J – V curves and EQE curves of the polymer solar cell devices: (a) conventional cell, (b) inverted cell, and (c) EQE curves of the (b) graph.

Table 1 Photovoltaic performances of P(BDP-DTPz):PC₇₁BM blends

| Device structures | PC ₇₁ BM ratios | V_{oc} [V] | J_{sc} [mA cm ⁻²] | FF [%] | PCE _{max} /PCE _{ave} ^a [%] |
|-------------------|----------------------------|--------------|---------------------------------|--------|---|
| Conventional | 1 : 1 | 0.838 | 8.1 | 63.8 | 4.5/4.4 ± 0.13 |
| Conventional | 1 : 1.5 | 0.838 | 8.7 | 65.0 | 4.8/4.7 ± 0.09 |
| Conventional | 1 : 2 | 0.838 | 7.9 | 58.8 | 4.0/3.8 ± 0.20 |
| Conventional | 1 : 3 | 0.838 | 6.9 | 58.9 | 3.5/3.3 ± 0.23 |
| Conventional | 1 : 4 | 0.838 | 6.3 | 57.6 | 3.1/2.8 ± 0.31 |
| Inverted | 1 : 1.5 | 0.858 | 9.2 | 63.4 | 5.1/4.9 ± 0.17 |
| Inverted (PFN) | 1 : 1.5 ^a | 0.859 | 11.1 | 65.3 | 6.2/6.1 ± 0.11 |

^a The average PCE values are calculated from 10 independent cells.

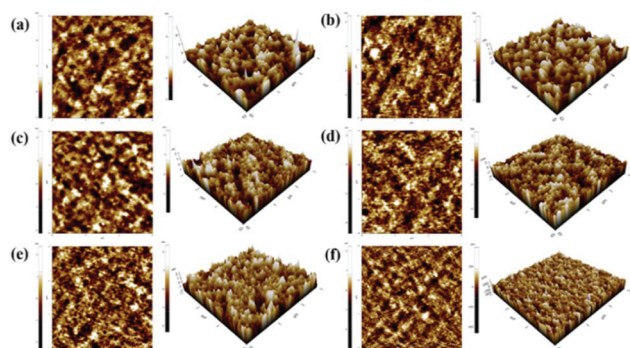


Fig. 7 AFM images of the P(BDP-DTPz):PC₇₁BM blend films processed by pure *o*-DCB, conventional cells: (a)–(e), inverted cell: (f).

PC₇₁BM ratios of 1:1 to 1:4, the PCE decreased as the amount of PC₇₁BM increased, with similar morphology changes being observed in the AFM images. As the PC₇₁BM ratio decreased, the phase of each film became smoother, as shown in (a)–(d), and the dark clusters of PC₇₁BM reduced to the nanoscale. As a result, electron movement between the polymer and PC₇₁BM became easier, resulting in an increase in J_{sc} , which finally led to improvements in device efficiency. The root mean square (RMS) values of (a), (b), (c), and (d) were 0.540 nm, 0.564 nm, 0.366 nm and 0.7 nm, respectively.

Fig. 7(e) shows the 1:1.5 polymer and PC₇₁BM film from the device that showed the highest PCE of the conventional cells (4.9%). As seen from the 2D and 3D topography images in (e), more micro-phases were found than when using ratios from 1:1 to 1:4, with nano-fibril structures that increased the surface area being observed, which eventually boosted the electron movement and provided high J_{sc} values. Moreover, the RMS value was 0.616 nm, 0.1 nm lower than that of the film of the 1:1 blended polymer and PC₇₁BM, which allows efficient electron movement. Lastly, as shown in Fig. 7(f), the 1:1.5 polymer:PC₇₁BM blend film on the ZnO + PFN hybrid inter-layer of the inverted cell displayed the smallest aggregation size, which allowed it to reach the effective exciton diffusion length in organic semiconductors. Overall, the ZnO + PFN layer resulted in a more homogeneous morphology in the active layer, and improved phase separation.⁵⁵ The RMS was 0.419 nm, 0.2 nm lower than that found in (e). Such factors led to the best PCE of 6.2%.

3.8.2 XRD and GI-WAXS analysis. To investigate the inter-chain packing structures of pristine and blend films, we also carried out XRD and GI-WAXS measurements. As shown in Fig. 8(a), in the out-of-plane direction the pristine film did not show the (100) peak related to the lamellar packing of the polymer, but there was a broad (010) peak around $2\theta = 20.98^\circ$. When using the value of 2θ in the Bragg's law equation ($\lambda = 2d \sin \theta$), the π - π stacking distance appears to be 4.19 Å. In other words, the polymer chain was stacked on the substrate with a face-on orientation, with the absence of the in-plane (100) peaks confirming the dominant face-on orientation of the polymer. The polymer:PC₇₁BM blend in the out-of-plane

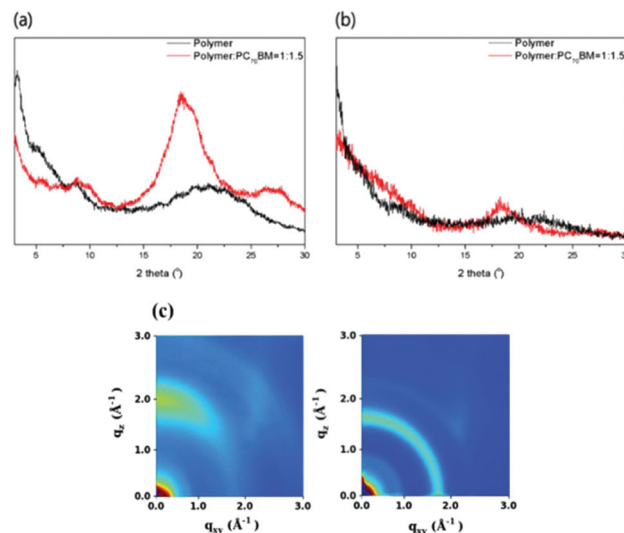


Fig. 8 XRD profiles of the polymer films in *o*-DCB: (a) out-of-plane, (b) in-plane and (c) GI-WAXS images; pristine film (on the left) and blend film (on the right).

direction shown in Fig. 8(b) displayed poor short-range ordering, with a larger π - π stacking distance of 4.66 Å ($2\theta = 18.68^\circ$) due to intercalation of PC₇₁BM with the polymer chain.

The GI-WAXS measurements found a high-intensity peak at a q_z value of 2 in the out-of-plane direction of the pristine film, but none in the in-plane direction, as shown in Fig. 8(c). This confirms the strong π - π stacking of the polymer on the substrate with a dominant face-on orientation.³⁷ The polymer:PC₇₁BM blend in Fig. 8(c) only reveals the presence of a PC₇₁BM peak, as the π - π stacking of the polymer was disturbed after mixing the polymer and PC₇₁BM, which matches the XRD data. The planar curvature and rigid structure of the polymer lead to pristine films with high degrees of π - π stacking, but little interaction with PC₇₁BM in blended films. This is probably due to the closer distance between the side-chains or neighboring repeat units in the main backbone, where the spacing is not enough to allow intercalation of PC₇₁BM.⁴⁰

3.9 Charge carrier transport properties

Electron and hole mobilities were measured using the space charge limited current (SCLC) method, as illustrated in Fig. 9.

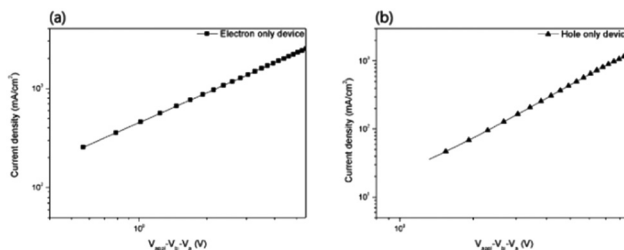


Fig. 9 SCLC; charge carrier mobility of the polymer: (a) electron mobility and (b) hole mobility.

The structure of the electron-only devices was ITO/ZnO/polymer:PC₇₁BM/Al, while that of the hole-only devices was ITO/PEDOT:PSS/polymer:PC₇₁BM/MoO₃/Ag, and the Mott–Gurney space charge limited current formula (eqn (1)) was used to calculate the mobility. Here, μ stands for charge carrier mobility, ϵ_0 and ϵ_r , the dielectric constant of free-space and the permittivity of the active layer, respectively, and V and L represent the applied voltage and thickness of the semiconductor layer, respectively.

$$J = \left(\frac{9}{8}\right) \mu \epsilon_0 \epsilon_r \left(\frac{V^2}{L^3}\right) \quad (1)$$

The electron mobility of the polymer was $5.9 \times 10^{-4} \text{ cm}^2 \text{ V}^{-1} \text{ s}^{-1}$, while the hole mobility was $3.3 \times 10^{-4} \text{ cm}^2 \text{ V}^{-1} \text{ s}^{-1}$. The balance ratio of polymer's electron mobility to hole mobility appears to be 0.56, and thus electrons move to each electrode in an efficient manner. This agrees with the photovoltaic properties and film morphology discussed above.

4. Conclusions

In this study, the optimization geometry of the D–A copolymer was calculated using the MM2 & MMFF94 function and non-covalent conformational locking, and its curvature was predicted. According to the theoretical calculation results, the backbone conformation and curvature of designed P(BDP-DTPz) could be found more easily than when using Gaussian 09, Jaguar quantum chemistry, Material Studio, etc. The P(BDP-DTPz) data predicted from the MM2 & MMFF94 function revealed differences in the tilting angles between the segments, but returned the results that were very similar to those obtained from the Gaussian 09 calculation. The synthesized polymer had a molecular weight and molecular weight distribution of $32\,542 \text{ g mol}^{-1}$ and 3.10, respectively, and a low band gap of 1.80 eV along with a broad absorption range after a 45 nm red-shift due to high aggregation in the thin-film phase. As designed, the HOMO level of P(BDP-DTPz) appeared as deep as -5.55 eV , and the face-on orientation was dominant in polymer films due to the planar curvature and rigid structure, showing closed packing with a π – π stacking distance of 4.19 \AA .

After characterizing the photovoltaic properties of P(BDP-DTPz), the highest efficiency was achieved when using a polymer:PC₇₁BM ratio of 1 : 1.5, and the optimized conditions and structure returned the best PCE of 6.2%, with a V_{oc} of 0.859 V, a J_{sc} of 11.1 mA cm^{-2} , and a FF of 65.3%. This appears to be the result of efficient mixing of the polymer with PC₇₁BM because of the smooth surface and the small, nanoscale domain size. This work will provide a new perspective for molecular design of D–A copolymers in PSCs.

Acknowledgements

This research was supported by the New & Renewable Energy Core Technology Program of the Korea Institute of Energy

Technology Evaluation and Planning (KETEP) grant funded by the Ministry of Trade, Industry & Energy (MI, Korea) (no. 20153010140030).

Notes and references

- 1 T. Kim, J.-H. Kim, T. E. Kang, C. Lee, H. Kang, M. Shin, C. Wang, B. Ma, U. Jeong, T.-S. Kim and B. J. Kim, *Nat. Commun.*, 2015, **6**(8547), 1–7.
- 2 T. Xu and L. Yu, *Mater. Today*, 2014, **17**, 11–15.
- 3 G. Li, V. Shrotriya, J. Huang, Y. Yao, T. Moriarty, K. Emery and Y. Yang, *Nat. Mater.*, 2005, **4**, 864–868.
- 4 L. Huo, T. Liu, X. Sun, Y. Cai, A. J. Heeger and Y. Sun, *Adv. Mater.*, 2015, **27**, 2938–2944.
- 5 S. Zhang, M. A. Uddin, W. Zhao, L. Ye, H. Y. Woo, D. Liu, B. Yang, H. Yao, Y. Cui and J. Hou, *Polym. Chem.*, 2015, **6**, 2752–2760.
- 6 Y. Liu, J. Zhao, Z. Li, C. Mu, W. Ma, H. Hu, K. Jiang, H. Lin, H. Ade and H. Yan, *Nat. Commun.*, 2014, **5**(5293), 1–8.
- 7 Y. Tamai, H. Ohkita, H. Benten and S. Ito, *J. Phys. Chem. Lett.*, 2015, **6**, 3417–3428.
- 8 B. Carsten, J. M. Szarko, H. J. Son, W. Wang, L. Lu, F. He, B. S. Rolczynski, S. J. Lou, L. X. Chen and L. Yu, *J. Am. Chem. Soc.*, 2011, **133**, 20468–20475.
- 9 W. Yue, R. S. Ashraf, C. B. Nielsen, E. Collado-Fregoso, M. R. Niazi, S. A. Yousaf, M. Kirkus, H. Y. Chen, A. Amassian, J. R. Durrant and I. McCulloch, *Adv. Mater.*, 2015, **27**, 4702–4707.
- 10 M. A. Uddin, T. H. Lee, S. Xu, S. Y. Park, T. Kim, S. Song, T. L. Nguyen, S. J. Ko, S. Hwang, J. Y. Kim and H. Y. Woo, *Chem. Mater.*, 2015, **27**, 5997–6007.
- 11 B. Meng, Y. Fu, Z. Xie, J. Liu and L. Wang, *Macromolecules*, 2014, **47**, 6246–6251.
- 12 W. Huang, E. Gann, L. Thomsen, C. Dong, Y. B. Cheng and C. R. McNeill, *Adv. Energy Mater.*, 2015, **5**, 1–11.
- 13 Y. Chen, S. Zhang, Y. Wu and J. Hou, *Adv. Mater.*, 2014, **26**, 2744–2749.
- 14 Y. Wu, Z. Li, W. Ma, Y. Huang, L. Huo, X. Guo, M. Zhang, H. Ade and J. Hou, *Adv. Mater.*, 2013, **25**, 3449–3455.
- 15 J. W. Jung, F. Liu, T. P. Russell and W. H. Jo, *Adv. Mater.*, 2015, **27**, 7462–7468.
- 16 S. Nam, J. Seo, S. Woo, W. H. Kim, H. Kim, D. D. C. Bradley and Y. Kim, *Nat. Commun.*, 2015, **6**, 1–9.
- 17 E. Zhou, K. Hashimoto and K. Tajima, *Polymers*, 2013, **54**, 6501–6509.
- 18 L. Yang, H. Zhou and W. You, *J. Phys. Chem. C*, 2010, **114**, 16793–16800.
- 19 J. Lee, J. H. Kim, B. Moon, H. G. Kim, M. Kim, J. Shin, H. Hwang and K. Cho, *Macromolecules*, 2015, **48**, 1723–1735.
- 20 N. Chakravarthi, K. Gunasekar, C. S. Kim, D. H. Kim, M. Song, Y. G. Park, J. Y. Lee, Y. Shin, I. N. Kang and S. H. Jin, *Macromolecules*, 2015, **48**, 2454–2465.
- 21 S. Liu, X. Bao, W. Li, K. Wu, G. Xie, R. Yang and C. Yang, *Macromolecules*, 2015, **48**, 2948–2957.

- 22 F. Livi, N. K. Zawacka, D. Angmo, M. Jørgensen, F. C. Krebs and E. Bundgaard, *Macromolecules*, 2015, **48**, 3481–3492.
- 23 B. Xu, S. Noh and B. C. Thompson, *Macromolecules*, 2014, **47**, 5029–5039.
- 24 D. Qian, W. Ma, Z. Li, X. Guo, S. Zhang, L. Ye, H. Ade, Z. Tan and J. Hou, *J. Am. Chem. Soc.*, 2013, **135**, 8464–8467.
- 25 B. C. Schroeder, M. Kirkus, C. B. Nielsen, R. S. Ashraf and I. McCulloch, *Macromolecules*, 2015, **48**, 5557–5562.
- 26 C. Du, Y. Ji, J. Xue, T. Hou, J. Tang, S.-T. Lee and Y. Li, *Sci. Rep.*, 2015, **5**(16854), 1–13.
- 27 X. Lu, H. Hlaing, D. S. Germack, J. Peet, W. H. Jo, D. Andrienko, K. Kremer and B. M. Ocko, *Nat. Commun.*, 2012, **3**(795), 1–7.
- 28 W. Lee, H. Cha, Y. J. Kim, J. Jeong, S. Hwang, C. E. Park and H. Y. Woo, *ACS Appl. Mater. Interfaces*, 2014, **6**, 20510–20518.
- 29 R. Rieger, D. Beckmann, A. Mavrinskiy, M. Kastler and K. Müllen, *Chem. Mater.*, 2010, **22**, 5314–5318.
- 30 T. L. Nguyen, H. Choi, S.-J. Ko, M. a. Uddin, B. Walker, S. Yum, J.-E. Jeong, M. H. Yun, T. J. Shin, S. Hwang, J. Y. Kim and H. Y. Woo, *Energy Environ. Sci.*, 2014, **7**, 3040–3051.
- 31 K. Zhang, M. Chen, K. J. Drummey, S. J. Talley, L. J. Anderson, R. B. Moore and T. E. Long, *Polym. Chem.*, 2016, **7**, 6671–6681.
- 32 B. Xia, K. Lu, L. Yuan, J. Zhang, L. Zhu, X. Zhu, D. Deng, H. Li and Z. Wei, *Polym. Chem.*, 2015, **7**, 1323–1329.
- 33 L. Huo, X. Guo, Y. Li and J. Hou, *Chem. Commun.*, 2011, **47**, 8850–8852.
- 34 L. Huo, J. Hou, H. Y. Chen, S. Zhang, Y. Jiang, T. L. Chen and Y. Yang, *Macromolecules*, 2009, **42**, 6564–6571.
- 35 J. Yuan, J. Ouyang, V. Cimrová, M. Leclerc, A. Najari and Y. Zou, *J. Mater. Chem. C*, 2017, **5**, 1858–1879.
- 36 J. Yuan, L. Qiu, Z. Zhang, Y. Li, Y. He, L. Jiang and Y. Zou, *Chem. Commun.*, 2016, **52**, 6881–6884.
- 37 J. Lee, H. Ko, E. Song, H. G. Kim and K. Cho, *ACS Appl. Mater. Interfaces*, 2015, **7**, 21159–21169.
- 38 M. Li, W. Ni, X. Wan, Q. Zhang, B. Kan and Y. Chen, *J. Mater. Chem. A*, 2015, **3**, 4765–4776.
- 39 S. Li, B. Zhao, Z. He, S. Chen, J. Yu, A. Zhong, R. Tang, H. Wu, Q. Li, J. Qin and Z. Li, *J. Mater. Chem. A*, 2013, **1**, 4508–4515.
- 40 T. L. Nguyen, S. Song, S. J. Ko, H. Choi, J. E. Jeong, T. Kim, S. Hwang, J. Y. Kim and H. Y. Woo, *J. Polym. Sci., Part A: Polym. Chem.*, 2015, **53**, 854–862.
- 41 W. Zhuang, A. Lundin and M. R. Andersson, *J. Mater. Chem. A*, 2014, **2**, 2202–2212.
- 42 S. Sahu, M. Das and G. Krishnamoorthy, *Phys. Chem. Chem. Phys.*, 2016, **18**, 11081–11090.
- 43 D. Fazzi and M. Caironi, *Phys. Chem. Chem. Phys.*, 2015, **17**, 8573–8590.
- 44 X. Guo, Q. Liao, E. F. Manley, Z. Wu, Y. Wang, W. Wang, T. Yang, Y. E. Shin, X. Cheng, Y. Liang, L. X. Chen, K. J. Baeg, T. J. Marks and X. Guo, *Chem. Mater.*, 2016, **28**, 2449–2460.
- 45 T.-J. Lin and S.-T. Lin, *Phys. Chem. Chem. Phys.*, 2015, **17**, 4127–4136.
- 46 T. L. Nguyen, S. Xu, S. Hwang, C. E. Park and H. Y. Woo, *Chem. Mater.*, 2014, **26**, 2147–2154.
- 47 S. Hedström and P. Persson, *J. Phys. Chem. C*, 2012, **116**, 26700–26706.
- 48 H. J. Song, D. H. Kim, E. J. Lee, J. R. Haw and D. K. Moon, *Sol. Energy Mater. Sol. Cells*, 2014, **123**, 112–121.
- 49 M. H. Choi, K. W. Song, D. K. Moon and J. R. Haw, *J. Ind. Eng. Chem.*, 2014, **29**, 120–128.
- 50 H. J. Song, J. Y. Lee, E. J. Lee and D. K. Moon, *Eur. Polym. J.*, 2013, **49**, 3261–3270.
- 51 G. Li, Z. Lu, C. Li and Z. Bo, *Polym. Chem.*, 2015, **6**, 1613–1618.
- 52 T. Hu, L. Han, M. Xiao, X. Bao, T. Wang, M. Sun and R. Yang, *J. Mater. Chem. C*, 2014, **2**, 8047–8053.
- 53 S. Beaupré, M. Belletête, G. Durocher and M. Leclerc, *Macromol. Theory Simul.*, 2011, **20**, 13–18.
- 54 M. C. Scharber, D. Mühlbacher, M. Koppe, P. Denk, C. Waldauf, A. J. Heeger and C. J. Brabec, *Adv. Mater.*, 2006, **18**, 789–794.
- 55 E. J. Lee, S. W. Heo, Y. W. Han and D. K. Moon, *J. Mater. Chem. C*, 2016, **4**, 2463–2469.